Short communication

3D porous LiFePO$_4$/graphene hybrid cathodes with enhanced performance for Li-ion batteries

Jinli Yang[a], Jiajun Wang[a], Dongniu Wang[a], Xifei Li[a], Dongsheng Geng[a],
Guoxian Liang[b], Michel Gauthier[b], Ruying Li[a], Xueliang Sun[a,*]

[a] Department of Mechanical and Materials Engineering, University of Western Ontario, London N6A 5B7, Canada
[b] Phostech Lithium Inc., 1475, rue Marie-Victorin, St-Bruno, QC J3V 6B7, Canada

ARTICLE INFO

ABSTRACT

Three-dimensional porous self-assembled LiFePO$_4$/graphene (LFP/G) composite was successfully fabricated using a facile template-free sol–gel approach. Graphene nanosheets were incorporated into the porous hierarchical network homogenously, which greatly enhances the electrical conductivity and efficient use of the LiFePO$_4$ (LFP), leading to an outstanding electrochemical performance of the hybrid cathodes. The obtained LFP/G composite has a reversible capacity of 146 mAh g^{-1} at 17 mA g^{-1} after 100 cycles, which is more than 1.4 times higher than that of porous LFP (104 mAh g^{-1}). Moreover, the porous LFP/G composite also exhibits a desirable tolerance to varied charge/discharge current densities.

© 2012 Elsevier B.V. All rights reserved.

1. Introduction

Recently, Li-ion batteries (LIB) have been recognized as alternative energy sources for electrical vehicles (EVs) and hybrid electrical vehicles (HEVs) [1,2]. The pioneering work of Goodenough [3], demonstrated that LiFePO$_4$ is a desirable cathode material with outstanding features, such as low cost, environmental compatibility, high theoretical specific capacity, and especially, superior safety performance. Unfortunately, the slow rate of lithium ion diffusion and poor electrical conductivity ($\sim$10^{-9} S cm^{-1}) limit the practical use of LiFePO$_4$ in LIB for EVs and HEVs [4]. To improve Li-ion diffusion within LiFePO$_4$ and the LiFePO$_4$/FePO$_4$ interface, one effective approach is to design nanosized LiFePO$_4$ particles, which shortens the Li-ion insertion/extraction pathways [5–13].

However, this strategy adversely affects the tap density and volumetric energy density, hampering its use in industrial-scale technologies. Therefore, the development of unique geometrical structures, such as micro-sized three-dimensional (3D) porous architectures, is a feasible strategy because such networks provide a high tap density, and a porous structure which facilitates the fast and efficient transport of mass and charge [14]. In addition, the interconnected open pores of this structure favor electrolyte percolation into active materials and hence efficiently use of electrode material [15,16].

Carbon coating is the most common and effective way to enhance the electrical conductivity of LiFePO$_4$ (LFP) [13]. Various conductive additives have been reported in carbon/LFP to enhance its electrical conductivity [17–19]. For example, carbon nanotubes (CNTs) were used as a novel carbon source because of their excellent electrical conductivity and network structure [20]. In comparison with CNTs, graphene can offer an improved interfacial contact because of its superior conductivity, flexible structure, and more importantly, high surface area (theoretical value of 2630 m^2 g^{-1}) [21]. Such promising advantages make graphene a great potential material for use in LFP. Su et al. directly mixed graphene with LFP particles mechanically and produced a composite mixture with an improved electrochemical performance, but the graphene was not well dispersed within the mixture, which limited the enhancement in electrical conductivity [22]. Consequently, the creation of effective graphene conductive networks is crucial for fully utilizing this unique carbon material.

By combining the advantages of porous LFP and unique properties of graphene, herein, we develop a novel 3D hierarchical LiFePO$_4$–graphene (LFP/G) hybrid cathode with a porous structure using a facile template-free sol–gel route. Graphene nanosheets, integrated with porous LFP, create an effective electronically conducting network. The development of this network in LFP/G yields a much better electrochemical performance compared with pristine LFP.

2. Experimental

2.1. Synthesis

Graphene sheets used in this study were prepared through the thermal expansion of graphite oxide. The preparation methodology for these sheets has been described in another research paper [23]. In a typical sol–gel route of LFP/G, 20 mg of graphene nanosheets were firstly dispersed in 30 mL of water via strong ultrasonic agitation for 30 min. Then, 1.039 g of lithium dihydrogen phosphate and 2.449 g of iron(III) citrate were dissolved separately in 170 mL of water by stirring at 70 °C for 1 h. The two solutions were mixed together and dried at 70 °C for 24 h. The obtained xerogel was subsequently fired in an argon atmosphere at 700 °C for 10 h. For the preparation of pristine porous LFP, graphene nanosheets were not added, but all other preparation methods followed the same route.

2.2. Physical characterization

Scanning electron microscopy (SEM) imaging was carried out using a Hitachi S-4800 microscope with an operation voltage of 5 kV. Transmission electron microscopy (TEM) observations were performed with a Hitachi H-7000 microscope at an accelerating voltage of 100 kV. Raman scattering (RS) spectra were recorded on a HORIBA Scientific LabRAM HR Raman spectrometer system. The XRD analyses were conducted using a Rigaku rotating-anode X-ray diffractometer, which employs Co Kα radiation. Thermogravimetric analysis (TGA) curves were collected by using a Netzsch system with a heating rate of 10 °C min^{-1} in air.

2.3. Electrochemical measurements

The LFP/G powder was mixed with acetylene black and polyvinylidene fluoride (PVDF) with a weight ratio of 75:15:10 in N-methyl-2-pyrrolidone (NMP) solvent to produce the slurry. The resultant slurry, pasted on Al foil, was dried at 100 °C under vacuum for 24 h to form the working electrode. The coin cells (2032) were then assembled in a high purity argon-filled glove box using lithium metal as the anode and 1 M LiPF$_6$ (dissolved in a solvent consisting of 50% ethylene carbonate and 50% dimethyl carbonate by volume) as the electrolyte.

The electrochemical performance of the as-obtained samples was conducted galvanostatically at various rates at room temperature using a computer-controlled battery test system (Arbin BT-2000 Battery Test System) within a voltage range of 2.5–4.2 V (vs. Li$^+$/Li). Cyclic voltamograms (CV) measurements were performed on an electrochemical workstation (Potentiostat/Galvanostat/EIS (VMP3)) over the potential range of 2.5–4.2 V (vs. Li$^+$/Li) at a scanning rate of 0.1 mV s^{-1}.

3. Results and discussion

The approach for LFP/G composite, schematically illustrated in Scheme 1a, starts with the dispersion of graphene sheets in deionized water, proceeds with the self-assembly of graphene with the LFP precursor, and ends with the crystallization of the LFP/G precursors. CO and CO$_2$ were evolved from the degradation of these precursors through annealing, resulting in the formation of a porous 3D network to obtain the final LFP/G product. A 3D cross-sectional view of LFP formation is shown in Scheme 1b. Porous LFP was also prepared by the same procedure for the sake of comparison.

Fig. 1a and b displays the transmission electron microscopy (TEM) and scanning electron microscopy (SEM) images of graphene, respectively. As shown in the figures, the typical wrinkled graphene is composed of layered platelets. The micrographs of porous LFP composite are shown in Fig. 1c and d.

Because of the production of gases generated during the citric anion degradation and their subsequent expulsion from the LFP structure, the surface of the LFP particles demonstrates the formation of a porous architecture (Fig. 1c). A close view shows the presence of abundant small nanometer-sized apertures (Fig. 1d), indicating the formation of an interlaced pore system network. Fig. 1e and f shows the SEM images of self-assembled hybrid LFP/G composite. The incorporation of graphene nanosheets does not seem to affect the interlaced channels. Moreover, graphene nanosheets are embedded into the LFP uniformly (Fig. 1e), resulting from the homogeneous dispersion of graphene within the LFP precursor suspension. The SEM image obtained under increased magnification further demonstrates that graphene is intimately incorporated into porous LFP particles (Fig. 1f).

Fig. 2a compares the XRD patterns of the porous LFP with the LFP/G. Both patterns perfectly match the standard orthorhombic LiFePO$_4$ (JCPDS #40-1499), indicating that the obtained samples are of a high purity and exhibit a high crystallinity. Moreover, the addition of graphene has no effects on the crystal structure of LFP through Raman spectroscopy. The Raman spectra of both samples are shown in Fig. 2b. Strong Raman peaks at 213, 280, 393, 441, 587 and 650 cm^{-1} can be detected for LFP and LFP/G, which are assigned to the fingerprint peaks of orthorhombic symmetry LFP [24]. Two broad peaks at 1315 and 1584 cm^{-1} are attributed to the D band and the G band, respectively [25]. The calculated peak intensity ratio (I_D/I_G) is an indicator of the degree of disordering in the carbon found in the samples, where a higher I_D/I_G ratio indicates a greater degree of disorder in the carbon arrangement [26]. Compared with the I_D/I_G ratio of 1.63 for LFP, the LFP/G shows a ratio of 1.08, indicating that the presence of graphite carbon in LFP/G is higher than that in the pristine LFP, which can result in an increased electrical conductivity of pristine LFP.

The TGA curve is shown in the insert of Fig. 2b. The weight changes of the pristine LFP and LFP/G are 1.62% and 2.61%, respectively. Combining the weight gain from the formation of Li$_3$Fe$_2$ (PO$_4$)$_3$ and Fe$_2$O$_3$ upon heating in air [27], the weight loss gives a carbon content of 6% in LFP and 7% in LFP/G.

To examine the effectiveness of graphene nanosheets in improving the electrochemical performance of the electrode, the Li-ion insertion/extraction properties in LFP/G and LFP are compared, as shown in Fig. 3. A single pair of oxidation and reduction peaks is observed for both samples, confirming the occurrence of a single electron transfer reaction in all samples during cycling, as demonstrated in Fig. 3a. For porous LFP, the anodic oxidation occurs at 3.55 V, and the cathodic reduction appears at 3.32 V, corresponding to a 0.23 V potential interval. For LFP/G, the potential interval is 0.2 V. The reduced potential interval value represents improved reversibility and reactivity.

The charge–discharge profiles of the samples at 17 mA g^{-1} cycled in a potential window of 2.5–4.2 V (versus Li$^+$/Li) at room temperature are shown in Fig. 3b. The performance discussed here is related to stable cycles. Typical flat plateaus over the voltage range of 3.4–3.5 V were obtained for both samples. Compared with porous LFP, LFP/G delivers higher charge and discharge capacities and a lower potential interval, indicating that porous LFP suffers from a larger polarization loss. The polarization between the charge and discharge plateau of the two samples increases along with an increase in the current density, as shown in the insert of Fig. 3b. More importantly, the potential interval is higher for LFP than LFP/G under various current densities, especially at higher current densities. As an example, the potential interval for LFP and LFP/G at a current density of 1700 mA g^{-1} is 812 mV and 362 mV, respectively. As an electrode has a lower electrical resistance with
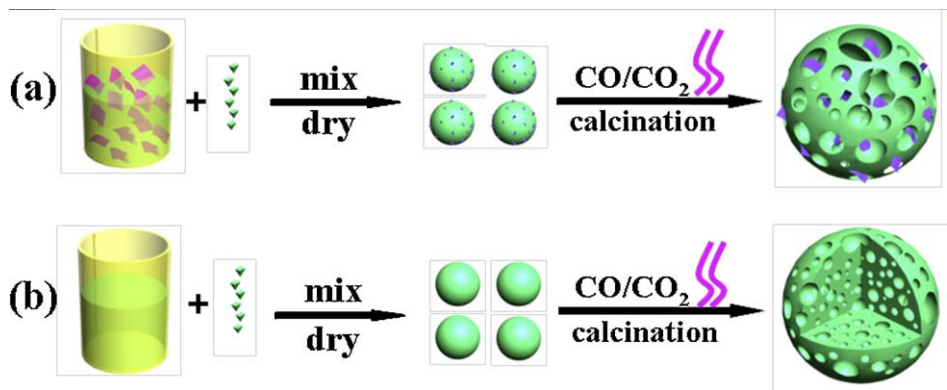
Scheme 1. Formation process of the 3D porous networks for (a) LiFePO₄/graphene and (b) LiFePO₄.

a lowered potential interval, these results indicate that graphene could potentially alleviate the polarization loss of LFP/G during the cycling. To examine the cyclic performance of porous LFP and LFP/G, long-term discharge cycling was performed at 17 mA g^{-1}.

The capacity stability was reached only after carrying out several initial cycles, and no detectable decline in capacity was observed over 100 discharge cycles for both samples, demonstrating that they have an excellent cycling performance, as shown in Fig. 3c.
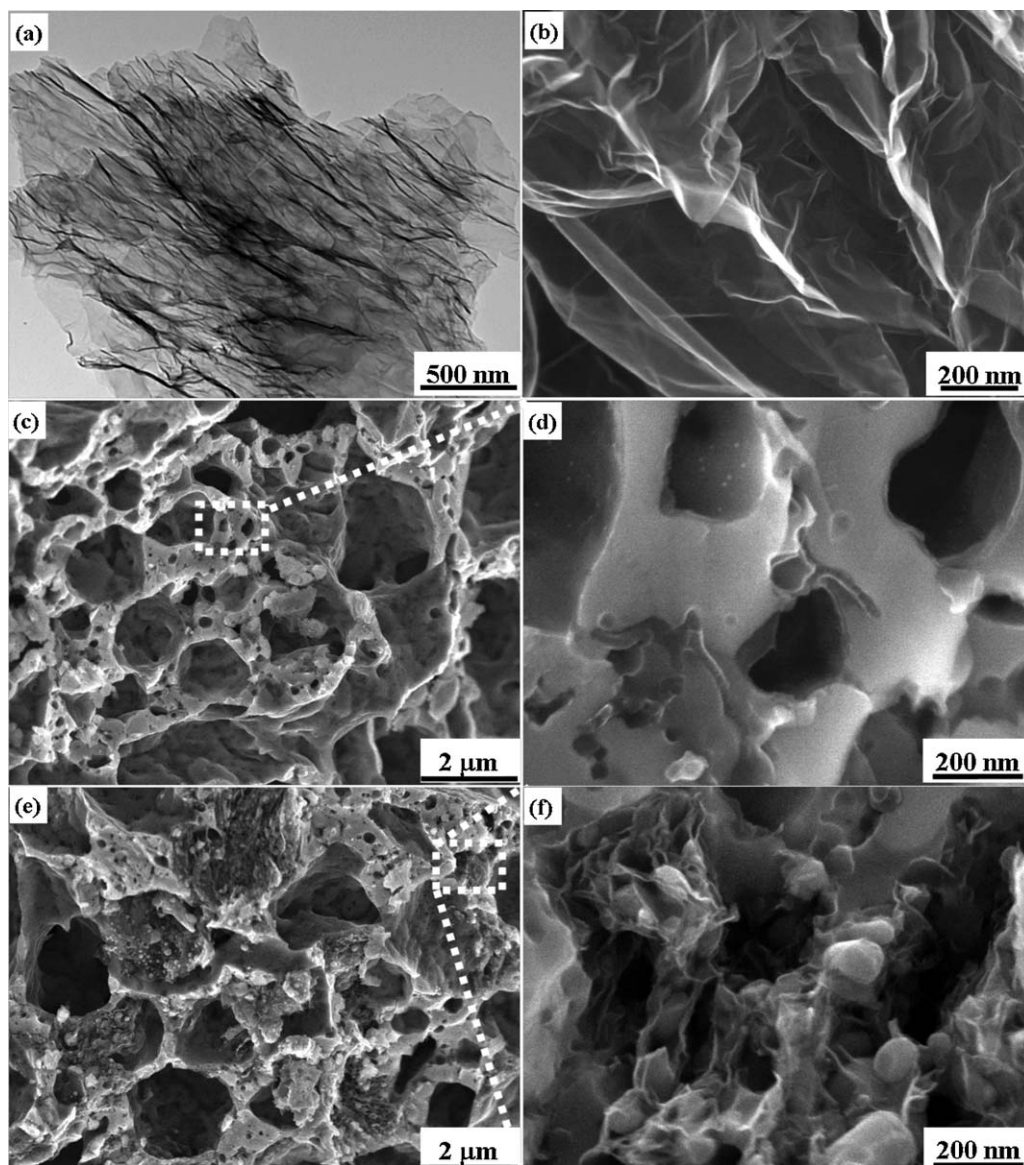
Fig. 1. TEM image of (a) graphene; SEM images of (b) graphene, (c) and (d) porous LiFePO₄ at different magnifications, (e) and (f) LiFePO₄/graphene composite at different magnifications.

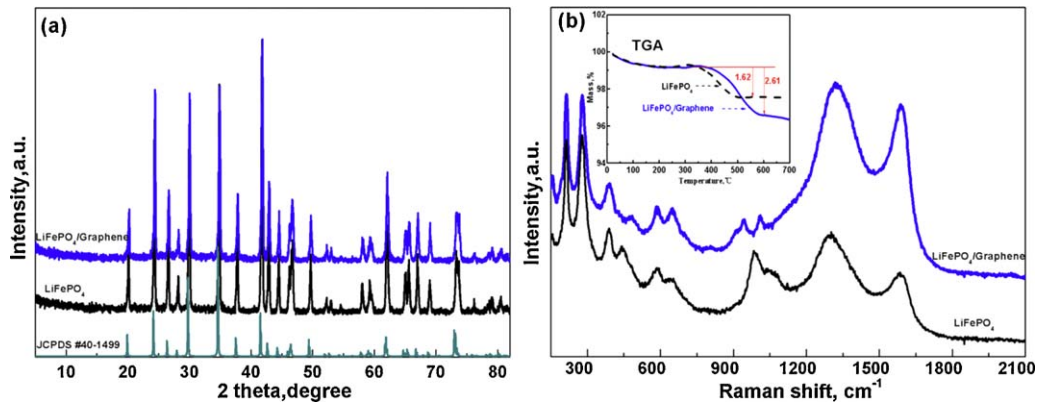**Fig. 2.** Powder X-ray diffraction (XRD) pattern (a), Raman spectra (b) and TGA curve of the inset of (b): porous LiFePO$_4$ and LiFePO$_4$/graphene composite.

After 100 cycles, LFP/G still delivered a capacity of 146 mAh g^{-1}, which is more than 1.4 times the capacity (104 mAh g^{-1}) of LFP, demonstrating that the incorporated graphene greatly enhances the specific capacity throughout the cycle process.

Fig. 3d compares the rate performance of porous LFP and LFP/G at different current densities. Under all charge/discharge rates, the specific capacities of LFP/G are higher than those of the porous LFP. The discharge capacity for LFP/G still remains stable at an extremely high current density of 1700 mA g^{-1}, while the capacity of LFP decreases significantly even at a lower rate of 340 mA g^{-1}. As long as the current density reverts back to a low current density of 17 mA g^{-1}, the original discharge capacity of LFP/G can be recovered, demonstrating that our 3D porous architecture LFP/G is tolerant to varied charge and discharge currents, which is a highly desirable property for electrode materials in lithium ion batteries.

The improvement can be ascribed to two main factors: graphene nanosheets possess a higher degree of graphitization than amorphous carbon, which increases the speed of electron migration, and embedded graphene nanosheets act as a bridge to increase the area that is simultaneously accessible to electrons and lithium ions, thus significantly reducing the inert zones and leading to high specific capacity [22].
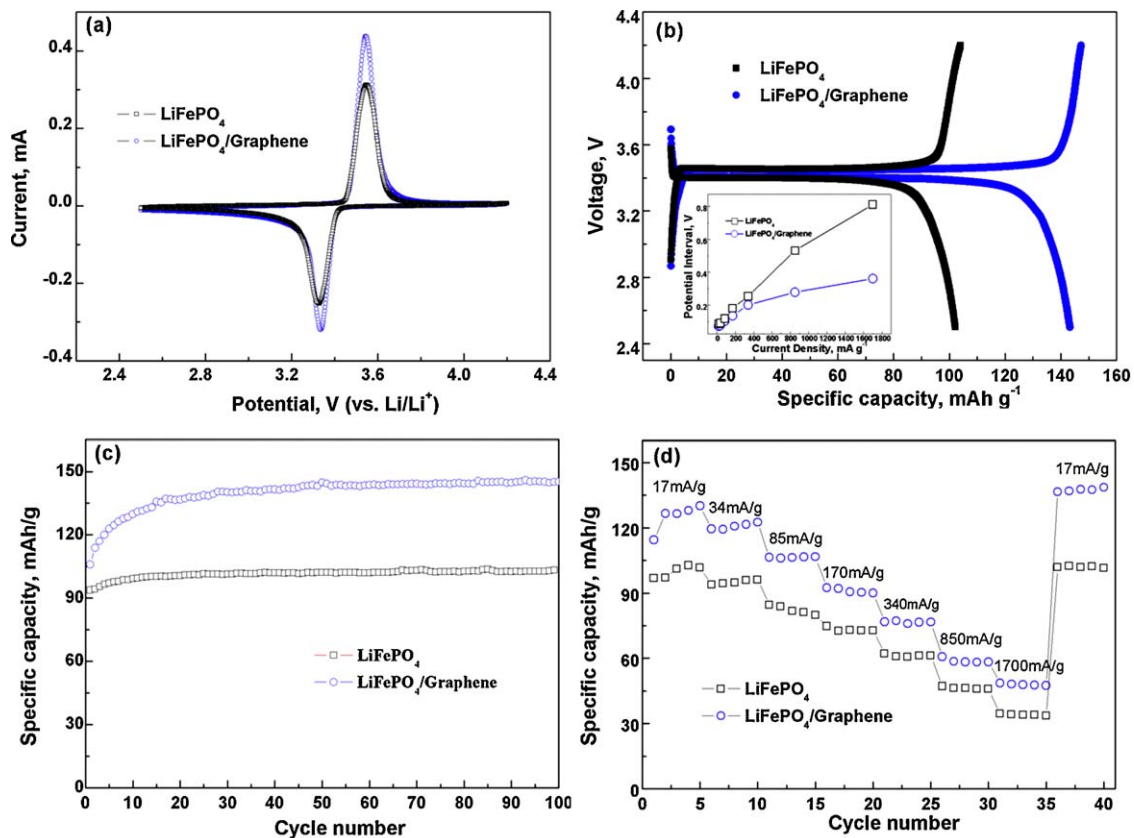

Fig. 3. (a) Cyclic voltammograms (0.1 mV s^{-1}). (b) Charge-discharge profiles of porous LiFePO$_4$, LiFePO$_4$/graphene cycled at a current rate of 17 mA g^{-1}. Inset: the potential interval of LiFePO$_4$ and LiFePO$_4$/graphene as a function of current density during the cycling. (c) Discharge capacities during continuous cycling of lithium cells at 17 mA g^{-1}; (d) rate performance.

4. Conclusions

In summary, we have successfully prepared a 3D hierarchical self-assembled LFP/G hybrid network using a facile template-free sol–gel method. Graphene nanosheets were dispersed uniformly into the porous structure, which led to the efficient use of the active materials. In comparison with porous LFP, the hybrid LFP/G composite shows significantly enhanced Li-ion insertion/extraction kinetics, which demonstrates that graphene nanosheets are promising conductive additives for Li-ion battery electrode materials. The self-assembly hybrid systems can also be applied to other hybrid structures to optimize the performance of electrodes in the energy storage system of electric or hybrid electric vehicles.

Acknowledgments

References

[1] J. Maier, Nat. Mater. 4 (2005) 805–815.
[2] J.M. Tarascon, M. Armand, Nature 414 (2001) 359–367.
[3] A.K. Padhi, K.S. Nanjundaswamy, J.B. Goodenough, J. Electrochem. Soc. 144 (1997) 1188.
[4] B.L. Ellis, W.R.M. Makahnouk, Y. Makimura, K. Toghill, L.F. Nazar, Nat. Mater. 6 (2007) 147–152.
[5] Y. Wu, Z. Wen, J. Li, Adv. Mater. 23 (2011) 1126–1129.
[6] J.S. Sakamoto, B. Dunn, J. Mater. Chem. 12 (2002) 2859–2861.
[7] M.S. Islam, D.J. Driscoll, C.A.J. Fisher, P.R. Slater, Chem. Mater. 17 (2005) 5085–5092.
[8] C. Delmas, M. Maccario, L. Croguennec, F.L. Cras, F. Weill, Nat. Mater. 7 (2008) 665–671.
[9] R. Dominko, M. Bele, J.M. Goupil, M. Gaberscek, M. Remskar, D. Hanzel, I. Arcon, J. Jamnik, Chem. Mater. 19 (2007) 2960–2969.
[10] Z.H. Chen, J.R. Dahn, J. Electrochem. Soc. 149 (2002) A1184–A1189.
[11] F. Yu, J. Zhang, Y. Yang, G. Song, J. Power Sources 189 (2009) 794–797.
[12] S.W. Oh, S.T. Myung, S.M. Oh, K.H. Oh, K. Amine, B. Scrosati, Y.K. Sun, Adv. Mater. 22 (2010) 4842–4845.
[13] J. Wang, X. Sun, Energy Environ. Sci. 5 (2012) 5163–5185.
[14] A. Magasinski, P. Dixon, B. Hertzberg, A. Kvit, J. Ayala, G. Yushin, Nat. Mater. 9 (2010) 353–358.
[15] Y.S. Hu, P. Adelhelm, B.M. Smarsly, S. Hore, M. Antonietti, J. Maier, Adv. Funct. Mater. 17 (2007) 1873–1878.
[16] W. Zhou, M. Yao, L. Guo, Y.M. Li, J.H. Li, S.H. Yang, J. Am. Chem. Soc. 131 (2009) 2959–2964.
[17] C.M. Doherty, R.A. Caruso, B.M. Smarsly, P. Adelhelm, C.J. Drummond, Chem. Mater. 21 (2009) 5300–5306.
[18] P.S. Herle, B. Ellis, N. Coombs, L.F. Nazar, Nat. Mater. 3 (2004) 147–152.
[19] D. Lepage, C. Michot, G.X. Liang, M. Gauthier, S.B. Schougaard, Angew. Chem. Int. Ed. 50 (2011) 6884–6887.
[20] Y. Zhou, J. Wang, Y. Hu, R. O'Hayreb, Z. Shao 46 (2010) 7151–7153.
[21] A. Peigney, C. Laurent, E. Flahaut, R.R. Bacsa, A. Rousset, Carbon 39 (2001) 507–514.
[22] S. Fang-Yuan, Y. Conghui, H. Yan-Bing, L. Wei, C. Wei, J. Fengmin, L. Baohua, Y. Quan-Hong, K. Feiyu, J. Mater. Chem. 20 (2010) 9644–9650.
[23] W.S. Hummers, R.E. Offeman, J. Am. Chem. Soc. 80 (1958) 1339.
[24] A.A. Salah, A. Mauger, K. Zaghib, J. Electrochem. Soc. 153 (2006) A1692–A1701.
[25] H. Hiura, T.W. Ebbesen, K. Tanigaki, H. Takahashi, Chem. Phys. Lett. 202 (1993) 509–512.
[26] T. Muraliganth, A.V. Murugan, A. Manthiram, J. Mater. Chem. 18 (2008) 5661–5668.
[27] I. Belharouak, C. Johnson, K. Amine, Electrochem. Commun. 7 (2005) 983–988.